



Energy Intensified Nitrogen Fixation Through Fast Modulated Gas Discharge from Pyramid-shaped Micro-electrode

Pradeep Lamichhane¹ · Nima Pourali¹ · Evgeny V. Rebrov^{1,2} · Volker Hessel^{1,3}

Received: 14 May 2023 / Accepted: 7 August 2023
© The Author(s) 2023

Abstract

Plasma-assisted nitrogen fixation has emerged as a promising alternative to conventional nitrogen fixation methods. In this study, we investigate the feasibility of plasma-assisted nitrogen fixation using an AC-driven dielectric barrier discharge generated from the micro-tips of a specially designed fast-modulated pyramid-shaped electrode. The obtained result is compared with the conventional flat electrode. Our results demonstrate that pyramid-shaped micro-tip electrodes can excite more nitrogen molecules than flat electrodes. Thus, pyramid electrodes have 58% more nitrogen oxides yield efficiency at 32% less energy cost. The highest nitrogen fixation is attained at 60% to 70% of oxygen concentration in nitrogen-feeding gas. These findings suggest that discharge through microtip is a promising and viable technology that could play a significant role in reducing the energy cost of the plasma-assisted nitrogen fixation method to meet the growing demand for sustainable nitrogen-based fertilizers.

Keywords Nitrogen fixation · Plasma · Micro-electrode · Energy yield · Energy cost · Micro-discharge

✉ Volker Hessel
volker.hessel@adelaide.edu.au

Pradeep Lamichhane
pradeep.lamichhane@warwick.ac.uk

Nima Pourali
nima.pourali@warwick.ac.uk

Evgeny V. Rebrov
e.rebrov@warwick.ac.uk

¹ School of Engineering, University of Warwick, Library Rd, Coventry CV4 7AL, UK

² Department of Chemical Engineering and Chemistry, Eindhoven University of Technology, De Zaal, Eindhoven 5600MB, The Netherlands

³ School of Chemical Engineering and Advanced Materials, University of Adelaide, North Terrace, Adelaide 5005, Australia

Introduction

Nitrogen is the fourth most prevalent element in a living cell after carbon, oxygen, and hydrogen [1]. Animals acquire nitrogen by consuming plants or other animals that have eaten plants, while plants obtain nitrogen from the soil. Despite the fact that our atmosphere is predominantly made up of nitrogen (about 78%), plants cannot directly absorb it from the air. Additionally, over-farming has led to the depletion of nitrogen from farmland, resulting in reduced crop yields [2]. One potential solution is to replenish the soil with nitrogen, but it must first be fixed through natural or artificial means [3, 4]. While natural nitrogen fixation occurs, it is not adequate to meet the demand, which has spurred researchers to concentrate on developing artificial nitrogen fixation techniques.

In 1903 AD, the Birkeland Eyde process was used to perform the first industrial nitrogen fixation by passing air through an electric arc to produce nitric acid [5, 6]. However, due to the high energy consumption (300–500 GJ/t) and limited renewable energy sources available at the time, this method was not sustainable [7, 8]. In 1908 AD, Nobel prize laureate Fritz Haber and Carl Bosch invented the Haber-Bosch (H-B) process [9]. In which, over an iron-based catalyst nitrogen reacts with hydrogen at 150–300 atm pressure and 400–500 °C temperature [10]. Following the industrial implementation of the H-B process in 1913 AD, a revolution was witnessed in the chemical industry sector. As of now, annual 140 million tons of ammonia are being synthesized by this process at an energy cost of 18 GJ/t to 100 GJ/t [7, 8], which accounts for 29% of total nitrogen fixed on Earth [11]. Approximately 80% of this ammonia is used to create fertilizers to feed 40% of the worldwide population [12]. Behind this, the H-B process consumes 2% of the worldwide petroleum which is 80% of the total energy used in the chemical industries. The H-B process is not only centralized and energy/cost-intensive, but it is also environmentally hazardous [13]. During the steam transformation of methane to generate hydrogen, more than 200 million tons of carbon dioxide (CO₂) gas is released which contributes 75% of the annual greenhouse gas emissions in the earth [10]. To overcome all these costs, energy, and environment-related issue, scientists are looking for an alternative sustainable and localized fixation technology.

Numerous studies on dielectric barrier discharge (DBD) have suggested that it may be a viable alternative to high temperatures and pressures for the redox transformation of nitrogen [14–22]. The energy impact collision between the molecular nitrogen and electrons has sufficient energy to break or weaken the nitrogen triple bond ($N \equiv N$) in DBD. The weakened triple bond can then be broken with successive collisions [23]. This atomic nitrogen can easily either oxidize into nitric oxides (NO), nitrite (NO₂), nitrate (NO₃), or reduced into ammonia (NH₃), which can all be used as fertilizers [24]. Theoretically, plasma-assisted nitrogen fixation has the lowest energy consumption rate (3–6 GJ/t) in comparison to other technology [8]. Besides this, it can operate in atmospheric conditions, uses sustainable energy, doesn't release greenhouse gases, is simple to use, and localized production (on-site, on-demand) is also conceivable [25].

Plasma-synthesized fertilizer is a cutting-edge advancement in agricultural technology that offers a sustainable and eco-friendly alternative to traditional chemical fertilizers. By using plasma technology, nitrogen from the air can convert into NO_x in the gas phase which is readily soluble in water, forming nitrite (NO₂⁻) and nitrate (NO₃⁻). These compounds can serve as a source of nitrogen for plants (nitrogen fertilizer), although directly using them as fertilizers is not a common practice because of their acidity. To make them more suitable and safe for agricultural use, they undergo a straightforward process of conversion into compounds like Ammonium Nitrate or other metal salts such as Calcium Nitrate or

Magnesium Nitrate [3]. These transformed forms of nitrite and nitrate are commonly utilized as fertilizers. This method not only reduces the environmental impact associated with the production and use of chemical fertilizers but also improves nutrient absorption by plants, leading to enhanced crop yields [26–28]. Additionally, plasma can facilitate seed germination and accelerate plant growth, contributing to improved agricultural productivity. Moreover, plasma treatments have been found to increase the drought and stress tolerance of crops, making them more resilient to challenging environmental conditions. By leveraging the power of plasma, agriculture can transition towards a more efficient, sustainable, and eco-conscious approach, addressing global food security and environmental concerns [27].

The behavior and characteristics of a plasma can be significantly influenced by the shape of the electrode. Amri et al. (2019) have emphasized the importance of electrode shape, with specific attention to cylindrical, spiral, and screw types of electrodes for various applications [29]. In a recent study, Gilbert et al. (2022) investigated the effects of electrode width on the deposited power, induced flow, and spatial distribution of reactive species in a surface barrier discharge array. They found that decreasing electrode width led to an increase in power density and oscillatory flow [30]. Takayama et al. (2006) employed pyramid-shaped electrodes to reduce breakdown voltage and control ozone concentration by adding small pyramids to the surface of cylindrical electrodes [31]. Other researchers, such as Liu et al. (2014, 2013) and Takaki et al. (2004), have also investigated the effects of electrode shape, including the use of double hexagon needle-array electrodes and right-pyramid electrodes, respectively [32–34]. However, most of these studies focused on pointed electrode shapes that were not as sharp as those used in our experiment. Furthermore, the impact of sharp electrode shapes on nitrogen fixation has not been thoroughly explored in previous research.

In this study, we fabricated a charge injector DBD by engraving pyramid-shaped micro (μ) tips on the HV electrode. The sharp edges of these tips were expected to increase the rate of secondary electron and field emission, leading to higher vibrational states of nitrogen molecules. The excited nitrogen molecules can easily react with oxygen molecules at normal temperatures and pressure. Additionally, micro-electrode dielectric barrier discharges (μ -DBDs) are advantageous because they have high production efficiency. It is challenging and expensive to fabricate electrodes with very sharp tips. Therefore, when designing the structure, we made an effort to select the maximum sharp edge with the least financial burden. To evaluate the practical benefits of μ -DBDs, we compared the results of the pyramid μ -electrode DBD with a conventional flat electrode DBD.

Experimental Setup and Methodology

Two identical setups, flat electrode DBD, and pyramid μ -electrode DBD were used in the experiment. Photograph of flat and μ -tip pyramid containing HV electrode is shown in Fig. 1a and b, respectively. Pyramid tips were designed and fabricated by the University of Adelaide with the help of ANFF-SA, University of South Australia. To demonstrate charge injection phenomena, we engraved 160 regular pyramids in a periodic pattern on a Titanium coin. Dimensions and orientations of pyramids are shown in Fig. 1c and d. At a distance of 0.5 mm, there are pyramids with 1 mm² base 1 mm height. There are no infinitely sharp points that exist in reality and achieving extreme sharpness at atmospheric pressure is highly susceptible to damage. For our experiment, the curvature radius of the

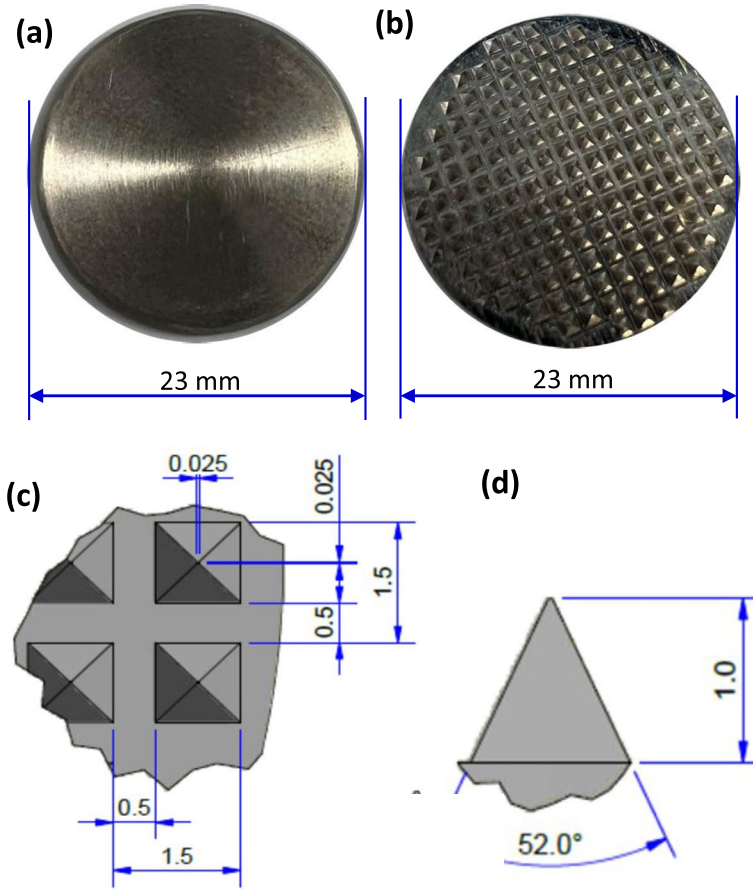


Fig. 1 A photograph of a **a** flat electrode and **b** pyramid array electrode. **c** Vertical and **d** horizontal view of pyramids and their dimensions

pyramid tip was set at 25 μm . This allowed us to strike a balance between achieving a sharp tip and avoiding excessive vulnerability to damage. These two flat and pyramid surfaces are connected to the HV electrode. Figure 2a presents the schematic diagram of the DBD plasma reactor used in the experiment, (b) shows a photograph of the plasma reactor, and (c) illustrates the peripheral of the reactor and all instrumental setups. To avoid the arcing in between the edge of the HV electrode and the ground electrode, the circular disc of the ground electrode covered by the dielectric layer is quite wider than the HV electrode. The ground electrode, covered with 200 μm thick dielectric layer (Mica sheet), was circular with a 25 cm diameter, while the HV disc had a 23 cm diameter to prevent arcing at the edge. Both electrodes were enclosed in a cylindrical quartz window with a sealed peripheral region.

The gap distance between the HV electrode and the ground electrode was maintained with the help of the adjustable screw located at the top of the HV electrode. The input gas was supplied from the back of the ground electrode, and the output gas was taken from the back of the HV electrode. To investigate the effect of different oxygen and nitrogen

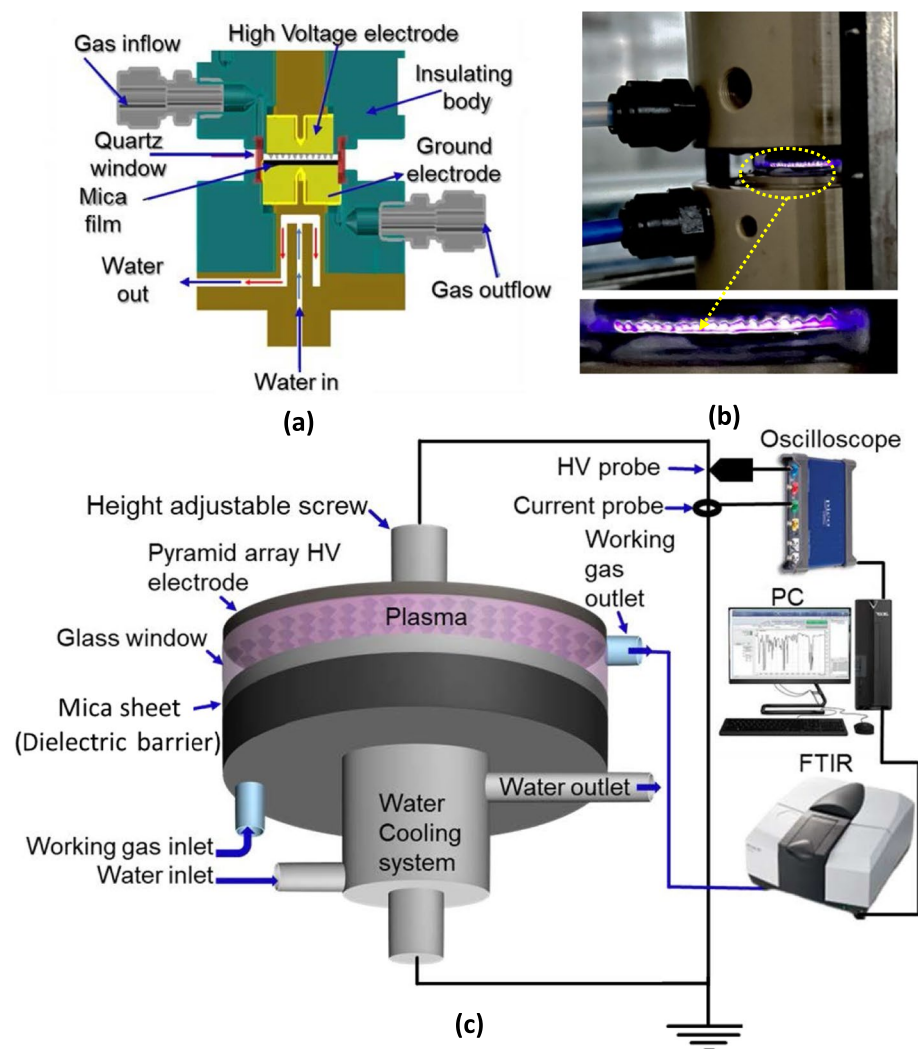


Fig. 2 Schematic of **a** interior of a plasma reactor, **b** photograph of the plasma reactor, and **c** plasma reactor morphology and instrumental setup

admixtures on plasma discharge chemistry, eight different conditions were studied by varying the oxygen and nitrogen flow rates while keeping the total flow rate constant at 140 sccm. Eight different oxygen concentrations in feeding gas [0 sccm O_2 + 140 sccm N_2 (0% O_2), 30 sccm O_2 + 110 sccm N_2 (22% O_2), 50 sccm O_2 + 90 sccm N_2 (36% O_2), 70 sccm O_2 + 70 sccm N_2 (50% O_2), 90 sccm O_2 + 50 sccm N_2 (64% O_2), 100 sccm O_2 + 40 sccm N_2 (71% O_2), 110 sccm O_2 + 30 sccm N_2 (78% O_2), and 140 sccm O_2 + 0 sccm N_2 (100% O_2)] were performed at 0.5 mm gap distance. Gas flow in the reactor was regulated using a Bronkhorst mass flow controller.

To maintain a constant temperature of 20 °C, water flow was regulated for the electrode. A 10 nF capacitor was introduced to the ground line for monitoring the electric charges generated in the plasma. Redline Technologies' G2000 high-voltage power generator

produced sinusoidal waves of varying amplitudes and frequencies, powering the plasma reactor at a fixed frequency of 68 kHz in this experiment. The Pearson 6600 current transformer and Tektronix P6015A 1000X high voltage probe were employed to measure current and voltage, respectively, and the signals were captured using a pico-tec oscilloscope (pico-scope 3000 series). The voltage and current signals were plotted in a two-dimensional graph to generate a Lissajous figure. The area of this figure was used to calculate the mean energy dissipation (power) during gas discharge.

Optical emission spectroscopy (OES) is used to analyze the elemental composition of a sample by measuring the light emitted by the sample when excited by an external energy source. Plasma excites the atoms and ions in the sample, causing them to emit light at specific wavelengths. The emitted light is then separated into different wavelengths by a spectrometer, allowing for the identification and quantification of the elements present in the sample. OES is a rapid and simple technique widely used for detecting reactive and excited species in the plasma phase. For this experiment, a Princeton Instruments FERGIE fiber optic spectrometer (FER-SCI-1024BX-UR) equipped with a 1200 lines/mm grating and a 25 μm slit width was used to cover a wide range (180–1100) with a resolution of ~ 0.26 nm. Light emission from the plasma was detected through an optical fiber located 5 mm perpendicular to the reactor window. Rotational temperature estimation was carried out by selecting rotational levels from the 0–2 vibrational band of $\text{N}_2 C^3\Pi_u(\nu = 0) - B^3\Pi_g(\nu = 0)$. The particular nitrogen rotational band has been provided in [35], and the process of estimating the rotational temperature is explained in detail in [36]. Similarly, to determine the vibrational temperature, OES intensities of $N_2^+(B - X)$ were utilized in the LIFBASE spectroscopic simulation software from SRI internationals.

Fourier transform infrared spectroscopy (FTIR) is a widely used technique for the analysis of the molecular composition of a sample by detecting the absorption or transmission of infrared light. The peaks visible in the FTIR spectrum correspond to the vibrational frequencies of the molecular bonds in the sample, allowing for the identification of the functional groups present. In this study, the NO_x (NO , NO_2) gas generated during the experiment was analyzed using FTIR with a SHIMADZU IRTracer-100 instrument. The plasma output gas was introduced into a thermogravimetric analyzer (TGA) equipped with a temperature controller module from Pike-Technology, USA (<https://www.piketech.com>). The evolved gases from the TGA at 20°C were passed through a heated transfer line into a flow cell with a 10 cm path length and 38.5 ml volume, which was placed inside the infrared spectrometer for analysis. This flow cell allows the continuous flow of sample gas into an infrared beam, and the transmittance of the sample gas through the path of the infrared beam is recorded. The transmittance of FTIR spectra with a resolution of 0.5 cm^{-1} , was only recorded once the signal had stabilized. Each FTIR spectrum is an average of these 16 scans and we analyzed 5 sets of scans. The concentrations of NO and NO_2 were measured using the standard calibration curve method. Following a similar approach employed by Hill et al. for the quantitative measurement of OH radicals [37]. In this experiment, FTIR spectra of various known concentrations of NO and NO_2 obtained from precision calibration gas mixtures were recorded along with their corresponding transmittance values. Afterward, we generated a calibration curve by plotting concentrations against transmittance data. Subsequently, we determined the concentrations of NO and NO_2 in the actual experimental samples by measuring their transmittance values, similar to the method used by Pei et al. [38].

The concentrations of NO and NO_2 in this experiment were expressed in mg/L. Where, $\text{mg/L} = [\text{parts per million (ppm)} \times \text{density in Kg/m}^3]/1000$. Accordingly, 1 mg/L of NO

corresponds to 746 ppm, while NO_2 is approximately equivalent to 488 ppm. The real-time synthesis rate of gas phase NO_x in g/hour is determined by multiplying the concentration of NO_x in g/L with the flow rate in L/hour. Finally, the energy yield for NO_x synthesis was calculated in grams per kilowatt-hour [g/kWh]. This was done by dividing the NO_x synthesis rate in g/hour by the power in kW, using Eq. 1.

$$E_{yield} = \frac{NO_x \text{ synthesis rate (g/hour)}}{\text{Power (kW)}} \quad (1)$$

In this experiment, the energy yield refers to the amount of NO_x produced in grams when one kilowatt-hour (1 kWh) of electricity is consumed, which is equivalent to 3.6×10^6 Joules. The reciprocal of the energy yield obtained from Eq. 1 represents the real-time energy cost of gas phase NO_x in kWh/g. To determine the energy cost in Joules per gram (J/g), the reciprocal of the energy yield is multiplied by 3.6×10^6 . To convert the energy cost from J/g to a more practical unit for large-scale processes, multiply it by 10^{-3} , which gives the energy cost in Giga Joules per ton of NO_x (GJ/tN).

Results and Discussions

Electrical Properties

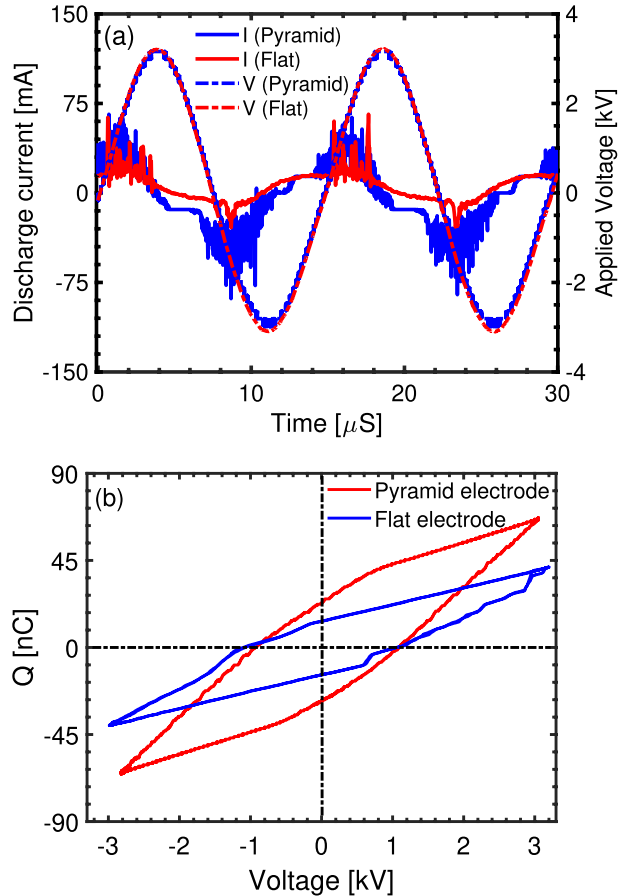
Figure 3 depicts current voltages waveforms of a typical AC-driven plasma source. There are several current peaks lasting a few milliseconds to nanoseconds during both the rising and declining sections of the applied voltage. Both plasma sources have identical discharge patterns, but the plasma with the pyramid μ -electrode has higher current peaks. The accumulation of wall charge ($Q = \int_0^T I_p dt$) during the positive half cycle of the applied voltage is diminished at the negative half cycle of applied voltage [3, 12]. After the positive and negative discharges, the wall charge decreases sharply with time, leading to an increase in gas resistance [6, 39]. The net charge transported over the course of a complete cycle is zero; thus, the QV plot (Lissajous figure) seems to be closed and it resembles a parallelogram as shown in Fig. 3(b). The area of the closed loop gives the mean energy dissipation (power) in plasma as given in Eq. 2 [40]. It is clearly seen that area of the Lissajous figure loop with a flat electrode is smaller than the pyramid μ -electrode which is due to the smaller current peaks in the flat electrode at the same applied voltage. Due to the ease of charge injection, pyramid μ -electrodes exhibit a higher peak discharge current compared to flat electrodes.

$$P = \frac{1}{T} \int_0^T I_p V_p dt = \frac{1}{T} \int_0^T I_m V_s dt = \frac{1}{T} \int_0^T V_s dQ. \quad (2)$$

Where T represents the time period ($=1/\text{Frequency}$); I_p denotes the plasma current; V_p indicates the voltages across the plasma gap; I_m refers to the monitoring current across the current transformer, and V_s represents the total applied voltage. In-depth calculations are available in the study by Pourali et al. [40].

Figure 4a shows the relationship between the mean energy dissipation and peak discharge current in both flat and pyramid μ -electrodes DBD plasma with varying oxygen admixtures. The peak height of current in the positive half cycle and the negative half cycle

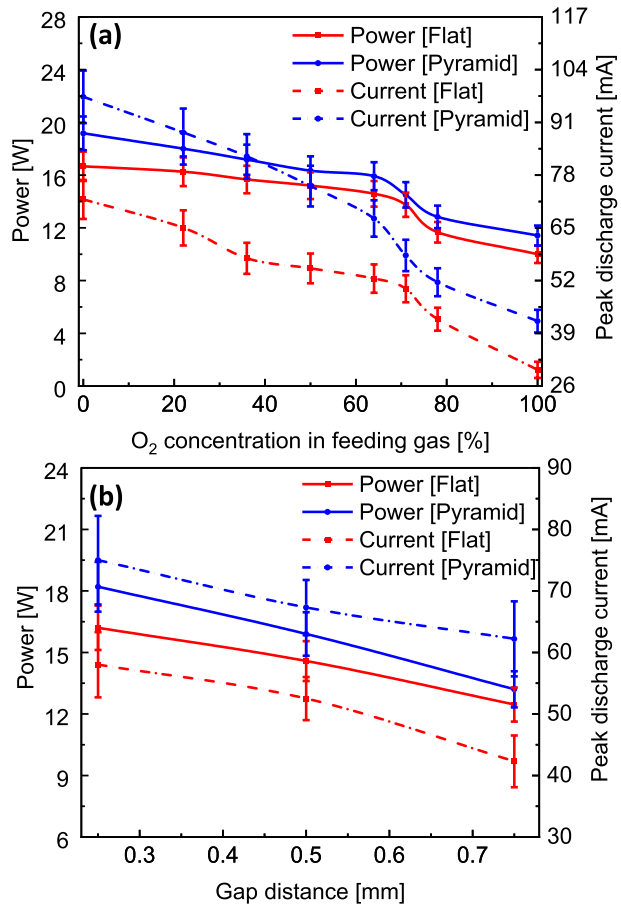
Fig. 3 a Typical current–voltage waveform of pyramid μ -electrode and flat electrode DBD and corresponding Lissajous figure. Both flat electrode and pyramid μ -electrode plasma were generated by the applied voltage of $V_{pp} = 6$ kV, frequency of 68 kHz, and working gas of 140 sccm with 50% of oxygen at gap distance of 0.5 mm



may not be equal. Thus, the current presented in this graph is the average of peak current in both directions. The results showed that the mean energy dissipation and peak discharge current exhibit a similar trend in both types of electrodes, declining as the concentration of oxygen in feeding gas increases. This can be attributed to the higher electronegativity of oxygen as compared to nitrogen. Oxygen has an electronegativity of 3.44 that of nitrogen is 3.04 [41]. As the oxygen concentration in nitrogen-feeding gas increases, primary ionization is expected to decrease. This decrease in peak current can be explained by the reduced primary ionization due to the electron affinity of oxygen [42]. Consequently, the reduced primary ionization leads to a decrease in mean dissipation energy.

In Fig. 4b, the relationship between mean energy dissipation and peak discharge current is depicted with respect to the gap distance between the HV electrode and ground electrode for both pyramid and flat electrodes DBD plasma, with a constant 64% oxygen admixture in nitrogen. The results show that as the gap distance increases, there is a decrease in peak discharge current and mean dissipation energy in both types of electrodes. This can be attributed to the inverse relationship between the intensity of the discharge current peak and the discharge length (plasma resistance) [23]. Additionally, the electric field decreases linearly with an increase in gap distance which also reduces the discharge current sharply at the same applied potential [43]. The decrease in mean energy dissipation with

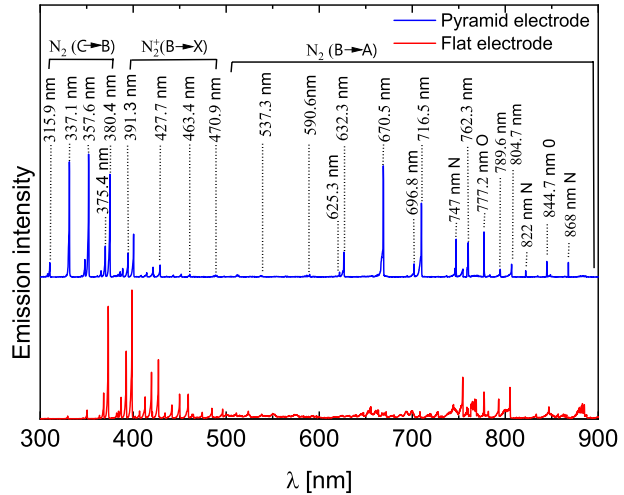
Fig. 4 Variation mean energy dissipation and peak discharge current with various **a** oxygen concentration in nitrogen main flow at 0.5 mm gap and **b** the gap distance between HV electrode and the ground electrode [Applied voltage of $V_{pp} = 6$ kV and frequency of 68 kHz]



an increase in the gap is attributed to the decrease in discharge current resulting from the reduced electric field and increased plasma resistance.

In Fig. 4b, the relationship between mean energy dissipation and peak discharge current is depicted with respect to the gap distance between the HV electrode and ground electrode for both pyramid and flat electrodes DBD plasma, with a constant 64% oxygen admixture in nitrogen. The results show that as the gap distance increases, there is a decrease in peak discharge current and mean dissipation energy in both types of electrodes. This can be attributed to the inverse relationship between the intensity of the discharge current peak and the discharge length (plasma resistance) [23]. Additionally, the electric field decreases linearly with an increase in gap distance which also reduces the discharge current sharply at the same applied potential [43]. The decrease in mean energy dissipation with an increase in the gap is attributed to the decrease in discharge current resulting from the reduced electric field and increased plasma resistance.

Fig. 5 The optical emission spectra of pure nitrogen plasma generated by flat (red) and pyramid μ -electrodes (blue) DBD. Both plasmas were produced using 140 cm with 50% of oxygen, with an applied voltage of $V_{pp} = 6$ kV, gap distance 0.5, and a frequency of 68 kHz (Color figure online)



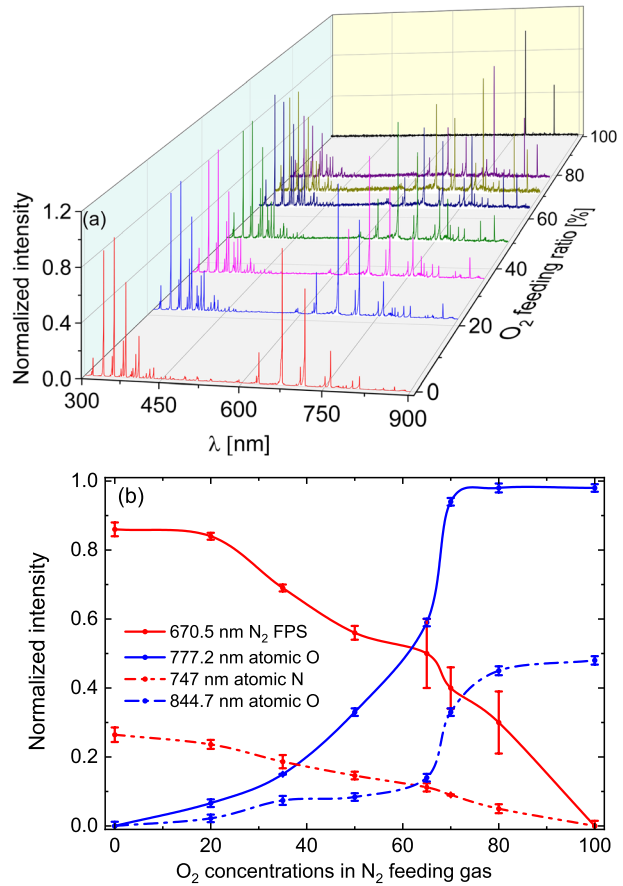
Optical Properties

OES of nitrogen plasma in the range of 300 nm to 900 nm obtained by both flat and pyramid μ -electrode DBD is shown in Fig. 5. In nitrogen plasma, the emission from 311 to 380 nm is mainly composed of N_2 second positive system (SPS), which corresponds to the transition $N_2(C^3 \Pi_g - B^3 \Pi_g)$ [44]. The emission from N_2 first negative system (FNS) was seen around 400 nm, which corresponds to the transition $N_2^+(B^2 \Sigma_u^+ - X^2 \Sigma_u^+)$ [44, 45]. Additionally, strong emission from N_2 first positive system (FPS), corresponding to the transition $N_2^+(B^3 \Pi_g - A^3 \Sigma_u)$ in the range of 478 nm to 900 nm [46–49], is mostly observed in pyramid μ -electrode DBD, making it different from the flat electrode DBD. Atomic nitrogen typically does not manifest in the OES spectrum of conventional DBD plasma. However, in the case of the pyramid-shaped μ -electrode, distinct emissions from atomic nitrogen have been observed at 747 nm, 822 nm, and 868 nm, which can be attributed to electron impact dissociation of nitrogen molecules ($N_2 + e \rightarrow 2N + e$). Based on a comparison with relevant literature [50–52], these emissions have been attributed to atomic nitrogen. Based on OES, it is evident that the pyramid μ -electrode produces a significantly higher amount of N_2 FPS and atomic nitrogen compared to conventional DBD plasma sources which are more advantageous for plasma-assisted nitrogen fixation.

In the OES of Fig. 5, there are several peaks of N_2 FPS in the spectrum. The strong emission peak is at 670.5 nm due to the vibrational transition [$v' - v''(\Delta v)$] of 5–2 (+ 3) [53, 54]. The other strong transition was at 632.3 due to a vibrational transition of 10–7 (+ 3) and at 716.5 due to a vibrational transition of 7–5 (+ 2). Activation of oxygen is also evidenced by the emission from atomic oxygen at 777.2 corresponding to the transition $3p^5P \rightarrow 3s^5S$ [51, 55] nm and 844.7 nm corresponding to the transition $3p^3P \rightarrow 3s^3S$ [51, 56, 57]. Characteristics of atmospheric-pressure non-thermal nitrogen and oxygen gas mixed DBD plasma is well described in the literature of Xiao et al [51]. Based on this research, the emission intensity of each gas depends on its corresponding feeding ratio.

Figure 6a illustrates the variation of OES in the pyramid electrode following the introduction of oxygen at different feeding concentrations. When oxygen is introduced, a portion of the electron energy is utilized to activate O_2 , leading to a decrease in the intensity of N_2 emission. Notably, at oxygen feeding ratios of 40–70% in conjunction

Fig. 6 Variation of optical emission **a** spectra and **b** intensities of pyramid μ -electrode with various oxygen concentrations in feeding gas. Plasma was generated by the applied voltage of $V_{pp} = 6$ kV, frequency of 68 kHz at a gap distance of 0.5 mm



with nitrogen feeding, there are moderate and almost equal proportions of both oxygen and nitrogen peaks. The changes in the peak OES intensities of 670.5 nm N_2 FPS, 747 nm atomic N, and 844.7 nm atomic O with various oxygen concentrations in pyramid μ -electrode DBD is also depicted in Fig. 6b. In this graph, OES intensity of the flat electrode is excluded because there is no significant peak of N_2 FPS at 670.5 nm and atomic nitrogen at 747 nm does not appear in the spectrum. Although the spectrum is primarily dominated by N_2 SPS in both plasma sources, we chose not to include it in the graph since its peak intensity remains consistently high even when the nitrogen concentration in the feeding gas is very low. This is due to its low activation energy. When the concentration of oxygen in the feeding gas increases, the N_2 FPS and atomic nitrogen present in the system gradually decrease over time, and atomic oxygen increases. Upon introduction of oxygen, a major portion of electron energy is utilized for activating O_2 because of its relatively low activation energies, ranging from 4.5 to 14.7 eV. As a consequence of the high electronegativity of oxygen, there is a high energy transfer from plasma (electrons) to oxygen, and less electron energy is available for activating N_2 molecules. This results in a decrease in the intensity of N_2 emission

with an increase in the O_2 content in the feeding gas. Notably, when the concentration of oxygen in the nitrogen-feeding gas is in the range of 60–75%, the emission intensities of atomic oxygen and atomic nitrogen are relatively high. Therefore, this gas mixture may potentially produce high levels of nitrogen oxides.

Thermal Properties

The thermal characteristics of plasma, such as the rotational temperature and vibrational temperature of nitrogen molecules, can provide valuable information about plasma discharge and energy transfer mechanisms. Due to the short rotational relaxation time of nitrogen, the rotational distribution of nitrogen in nitrogen-containing plasmas rapidly attains thermodynamic equilibrium, resulting in the exchange of rotational energy primarily with heavier particles instead of electrons. Therefore, the rotational temperature of nitrogen is usually assumed to be equal to the gas temperature in practical applications [36, 58]. The vibrational temperature of nitrogen is a measure of the thermal energy associated with the vibrational motion of nitrogen molecules [59]. One of the key non-equilibrium

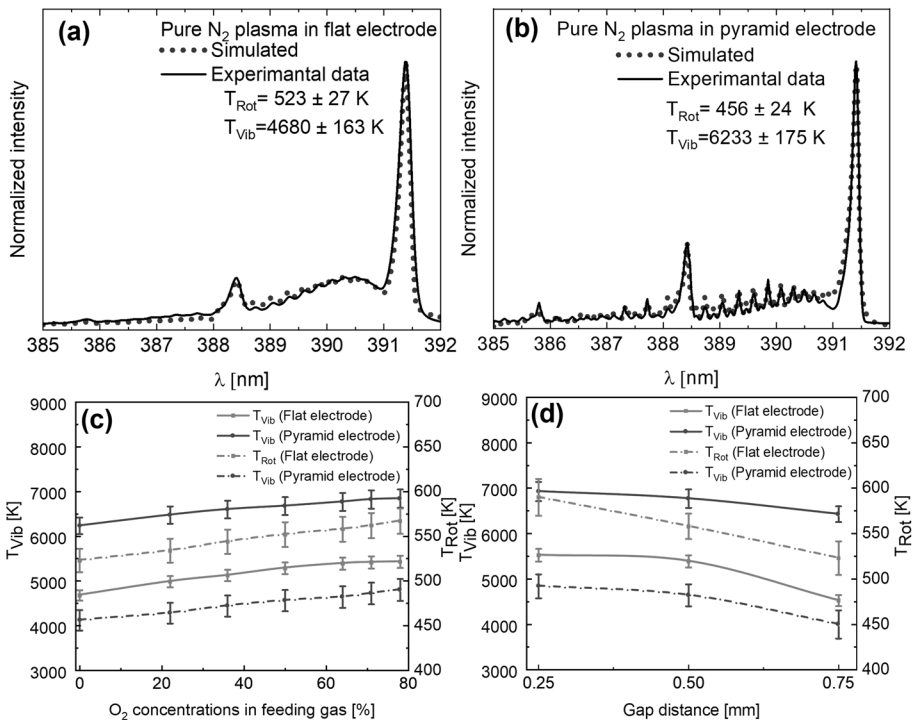


Fig. 7 Experimental and simulation spectra of the first negative system (FNS) ($N_2^+(B^2\Sigma_u^+ \rightarrow X^2\Sigma_g^+)$) for the determination of rotational temperature (T_{Rot}) and vibrational temperature (T_{Vib}) in **a** flat electrode and **b** pyramid μ -electrode. Plasmas were produced by 140 sccm of pure (99.999%) nitrogen. Variation of the rotational and vibrational temperature of pyramid μ -electrode and flat electrode DBD with various **c** oxygen concentrations in nitrogen feeding gas at 0.5 mm gap and **d** the gap distance between HV electrode and the ground electrode [Applied voltage of $V_{pp} = 6$ kV and frequency of 68 kHz]

characteristics of plasma is a higher vibrational temperature and lower rotational temperature. This ratio is important as it is more effective for redox reactions.

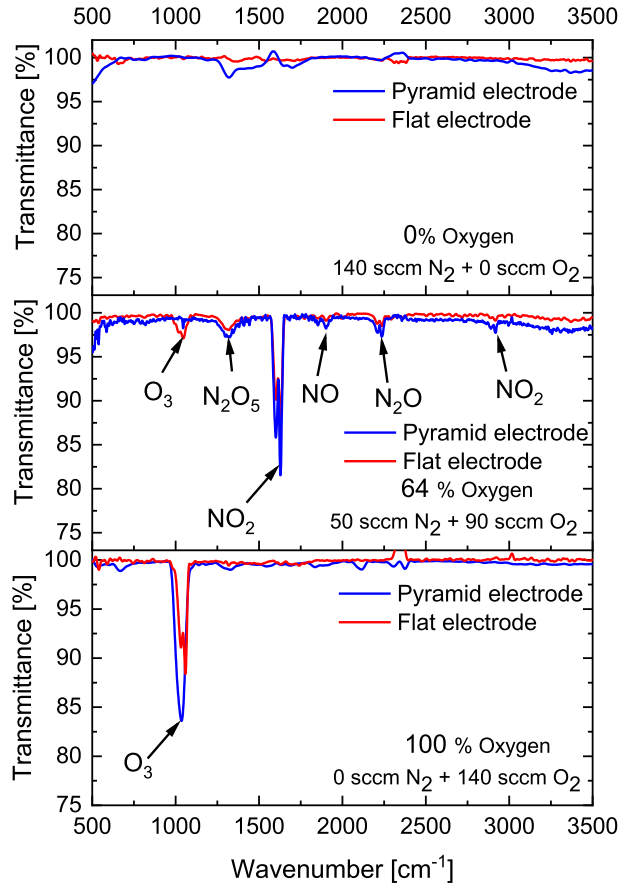
To evaluate the vibrational temperature, the experimental and simulation spectra of the FNS [$N_2^+(B^2\Sigma_u^+ \rightarrow X^2\Sigma_g^+)$] were scrutinized for both flat and pyramid μ -electrode DBD, as illustrated in Fig. 7a and b, respectively. The results showed that the vibrational temperature of pure nitrogen plasma in a flat electrode DBD with a gap distance of 0.5 mm was 4680 K, whereas, in the pyramid μ -electrode, it was 6233 K. At the same time, the rotational temperature of nitrogen in a flat electrode was 523 K, while in a pyramid μ -electrode DBD it was 456 K. The higher rotational temperature in the flat electrode plasma indicated that the flat electrode lost energy in the form of joule heating (thermal decomposition of species), while the higher vibrational temperature in the pyramid μ -electrode plasma indicated that more energy was used to dissociate N_2 molecules [59]. The electric field in a plasma discharge plays a crucial role in determining the energy distribution of charged particles and the population of different vibrational and rotational energy levels in the gas. The higher vibrational temperature in the pyramid μ -electrode can be attributed to the higher electric field, as the electric field is concentrated at the tip of the pyramid μ -electrode.

Figure 7c and d in the study demonstrate how the rotational and vibrational temperatures vary with different oxygen concentrations in feeding gas and gap distances in both flat and pyramid μ -electrode plasma. The results show that both rotational and vibrational temperatures increase as the oxygen concentrations increase, but decrease as the electrode gap distance increases. The increase in both rotational and vibrational temperatures with an increase in oxygen admixture is due to the transfer of kinetic energy from electrons to different rotational and vibrational levels of oxygen molecules [60, 61]. Oxygen has a higher electron affinity than nitrogen, so it tends to capture electrons, leading to an increase in the mean electron energy with increasing oxygen admixture. This increase in electron energy then leads to higher rotational and vibrational temperatures [59–61]. The decreasing trend of rotational and vibrational temperatures with an increase in gap distance may be due to the reduced electric field. A high population of vibrationally excited N_2 molecules leads to an enhanced dissociation of N_2 , which subsequently stimulates a higher synergistic chemistry in both the gas phase that actuates an efficient nitrogen fixation process. As the gap distance increases, the electric field decreases, leading to a reduction in the population of vibrationally excited N_2 molecules, and therefore, a decrease in the rotational and vibrational temperatures.

Fourier Transform Infrared Spectroscopy

FTIR spectra of gaseous products obtained from oxygen-mixed nitrogen plasma are displayed in Fig. 8. The spectrum of pure nitrogen is presented at the top of the figure. The FTIR spectrum of pure nitrogen gas shows no significant peaks related to nitrogen oxides. As the oxygen feeding increases, the intensities of NO , NO_2 , and N_2O_5 peaks increase significantly up to an oxygen concentration of 64% of oxygen. Beyond this point, the intensities of these peaks start to decrease. At 100% oxygen, the nitrogen oxide peaks vanish completely. The FTIR spectra of 64% oxygen are presented in the middle of the figure. The spectrum is dominated by NO_2 peaks in the region of 1660–1560 cm^{-1} . In parallel, N_2O peaks are found in the range of 2265–2145 cm^{-1} . Due to the strong stretch of NO_2 in N_2O_5 , another smaller peak appears in the regions of 1300–1350 cm^{-1} . NO peaks are observable in the range of 1965–1770 cm^{-1} . Ozone (O_3) peaks also appear in the spectrum at 1053–1125 cm^{-1} . The increasing concentration of ozone could be a contributing factor

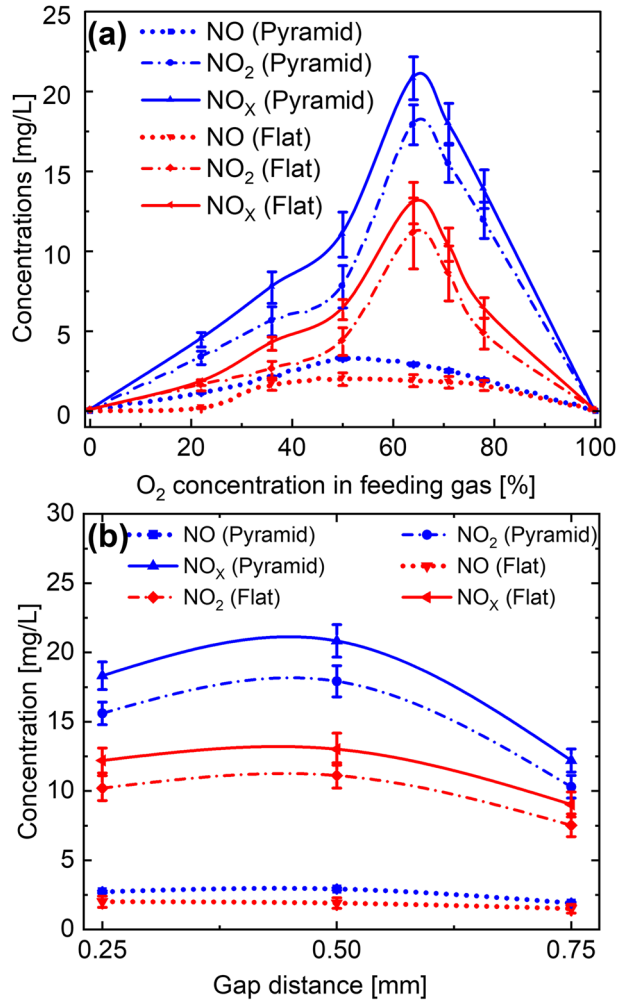
Fig. 8 FTIR spectra of gaseous products obtained from nitrogen plasma with various oxygen admixture. Plasma was generated by the applied voltage of $V_{pp} = 6$ kV and frequency of 68 kHz at a gap distance of 0.5 mm. Plasma was generated by the applied voltage of $V_{pp} = 6$ kV and frequency of 68 kHz at gap distance of 0.5 mm



to the rising amount of oxygen. Besides NO , NO_2 , other forms of nitrogen oxides such as dinitrogen pentoxide (N_2O_5) and nitrous oxide (N_2O) are also seen in the FTIR spectrum but these forms of nitrogen oxides are not taking into account because they are not our desired form of NO_x . Closely, the FTIR spectrum of pure oxygen plasma contains only ozone peaks, which are presented at the bottom of the figure.

The production of NO radical is crucial for the synthesis of other nitrogen oxide derivatives. When oxygen is present, the NO produced undergoes rapid oxidation to form relatively stable radicals known as NO_2 . The high concentration of NO_2 in the plasma is likely due to the presence of sufficient reactive oxygen species. In this experiment, the height of the NO_2 peaks ($1660\text{--}1560\text{ cm}^{-1}$) was found to be the highest in both flat and pyramid μ -electrode DBD plasma, but the pyramid μ -electrode DBD plasma had significantly higher peaks than the flat electrode DBD plasma. This may be attributed to differences in the electric field distribution in these two types of electrodes. Other nitrogen oxide peaks in both plasmas were very small and comparable to each other.

Fig. 9 Variation of NO_x production rate in the pyramid and flat electrode DBD with various **a** oxygen feeding concentration in nitrogen main flow and **b** the gap distance between HV electrode and the ground electrode at 64% oxygen in the main flow. Both flat electrode and pyramid μ -electrode plasma were generated by the applied voltage of $V_{pp} = 6$ kV and frequency of 68 kHz



Nitrogen Oxides Synthesis and Insights into the Chemistry

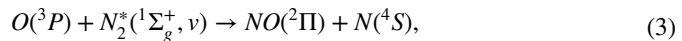
In Fig. 9a, the impact of oxygen concentration on the concentrations of NO , NO_2 , and total NO_x in the plasma output gas from flat and pyramid μ -electrode DBD is illustrated. Notably, NO concentration is considerably lower compared to NO_2 in both plasma types. The findings reveal that nitrogen oxide production is negligible in pure nitrogen plasma but steadily increases as the oxygen flow rate rises, reaching its peak, and then declining until it reaches zero with pure oxygen. Both NO and NO_2 follow the same trend, but the maximum NO concentration attained in the experiment is within the range of 40–50%. On the other hand, the maximum NO_2 concentration was observed at oxygen concentrations ranging from 60% to 70%. The maximum NO concentration obtained in this experiment was 50%, which corresponded to 3.2 mg/L (2388 ppm) from the pyramid electrode and 2 mg/L (1492 ppm) from the flat electrode. However, the maximum NO_2 concentration was observed at 64% of oxygen in this experiment which was 11.11 mg/L (5419 ppm) from the

flat electrode and 17.9 mg/L (8731 ppm) from the pyramid electrode. Consequently, the total NO_x remained highest within this range, primarily due to the higher concentrations of NO_2 .

At 22% of oxygen concentration, total NO_x concentration was measured to be 1.78 mg/L with the flat electrode and 4.46 mg/L with the pyramid electrode. These concentrations represent the conversion of 0.06% and 0.15% of the total nitrogen feeding into NO_x with the flat and pyramid electrodes, respectively. The maximum NO_x concentrations of 13.18 mg/L and 20.83 mg/L were observed at 64% oxygen concentration in the feeding gas with the flat and pyramid electrodes, respectively. This corresponds to 0.94% of nitrogen from the flat electrode and 1.54% from the pyramid electrode being converted into NO_x out of the 36% of nitrogen feeding. At 78% oxygen concentration, although the nitrogen fixation was lower compared to 64% oxygen (which was 13.88 mg/L with the flat electrode), the highest amount of nitrogen was converted to NO_x . Specifically, at this oxygen concentration, 1.65% of nitrogen was converted into NO_x . When oxygen concentrations are higher, there is a reduced amount of available nitrogen, causing a significant portion of the nitrogen to be converted into NO_x , despite lower observed NO_x concentrations in this range.

Figure 9b shows the variation in NO , NO_2 , and total NO_x concentrations with the gap distance between the HV electrode and ground at a fixed oxygen feeding concentration of 64%. In the course of the experiment, when the gap distance between the electrodes was extended from 0.25 mm to 0.50 mm, in both cases with flat and pyramid μ -electrodes, a marginal rise in the concentrations of NO_x was observed. Upon further widening the gap distance to 0.75 mm, a drastic reduction in NO_x concentrations was observed, regardless of the electrode configuration used. The results indicate that the maximum NO_x concentrations were obtained at an intermediate gap distance, and the concentrations were low at both high and low gap distances. Both reactors had their respective highest NO_x concentrations at a gap distance of 0.5 mm. The low production at a low gap distance could be attributed to the smaller plasma volume and residence time, while the low production at a higher gap distance could be attributed to the lower electric field.

In DBD, the electron temperature is in the range of 1 to 10 electron volts [62]. The vibrational excitation energy of nitrogen molecule ($v = 1$) is only 0.3 eV, while the dissociation energy is 9.8 eV, and ionization potential is 15.6 eV [63, 64]. The minimum energy required for plasma-assisted N_2 oxidation is determined by the energy available for nitrogen and oxygen excitation. Molecular $N \equiv N$ and $O = O$ bond is getting excited or broken via vibrational excitation, followed by a secondary exothermic process to form NO through the Zeldovich reactions as shown in Eqs. 3 and 4 [65, 66].

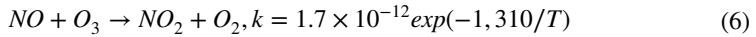


The formed NO immediately oxidized in to NO_2 because of the short lifetime (1.4 μ s) [67], as explained in Eq. 5 [18, 53, 68, 69].



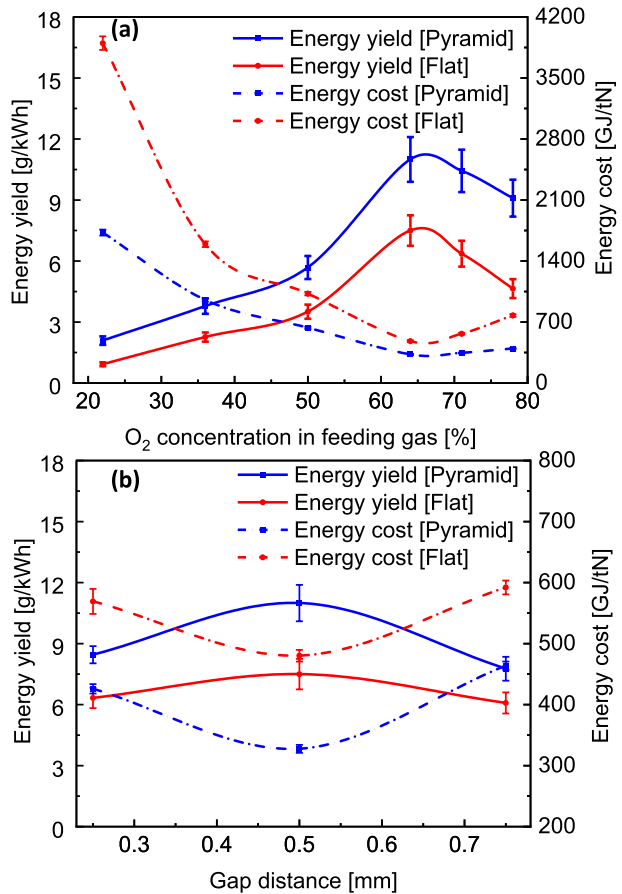
When a plasma is formed in the presence of oxygen, the high-energy electrons in the plasma can cause the dissociation of oxygen molecules into two individual oxygen atoms [$O(^3P)$]. These oxygen atoms are highly reactive and can readily react with other oxygen

molecules to form ozone (O_3) [70]. In O_3 , oxygen atoms have unpaired electrons and are therefore highly reactive with an oxidative potential of 2.07 V. The formed O_3 can easily oxidize nitrogen as explained in Eq. 6 [71].



Ozone can also be formed by three body reactions of metastable nitrogen, molecular oxygen, and atomic oxygen ($O_2 + O + M \rightarrow O_3 + M$) However when NO is present, the concentration of ozone cannot increase linearly with the oxygen flow rate. This is because ozone and NO can react with each other to form NO_2 and O_2 , which are relatively stable compounds [71]. This reaction reduces the concentration of both ozone and NO in the system. This phenomenon is important to consider in plasma-assisted nitrogen fixation processes, where the coexistence of ozone and NO is common. In such cases, the production of NO_2 is prioritized over the formation of ozone due to the reaction between ozone and NO . This can have an impact on the efficiency of ozone generation and the subsequent nitrogen fixation process. Therefore, it is crucial to take into account the effects when designing and optimizing plasma-assisted nitrogen fixation systems.

Fig. 10 Variation of energy yield and energy cost (red line) in the pyramid and flat electrode DBD with various **a** oxygen concentration in nitrogen flow and **b** the gap distance between HV electrode and the ground electrode at 64% oxygen feeding in the main flow. Both flat electrode and pyramid μ -electrode plasma were generated by the applied voltage of $V_{pp} = 6$ kV and frequency of 68 kHz (Color figure online)



Energy Yield and Energy Cost

The impact of variations in oxygen concentration in nitrogen-feeding gas on energy yield and cost for synthesizing NO_x using pyramid and flat electrodes is demonstrated in Fig. 10a. Higher production rates lead to increased energy yield, while increased power consumption leads to decreased energy yield. Despite its higher power consumption, the pyramid μ -electrode results in a higher energy yield than the flat electrode due to its higher NO_x production rate. Energy yield increases with an increase in oxygen admixture up to 60–70% of oxygen in the main feeding gas, after which it declines. The highest energy yield of 10.99 g/kWh was achieved at 64% of oxygen in the main feeding gas from the pyramid μ -electrode, which was only 7.5 g/kWh from the flat electrode. The energy costs were also minimum in both plasma sources within 60–70% of oxygen in the main feeding, while below and above this range, energy costs start to increase significantly. The pyramid μ -electrode with 64% of oxygen gives the minimum energy cost of 327.5 GJ/tN, compared to 480.2 GJ/tN in the flat electrode.

Variation of energy yield and energy cost with different gap distances at a 64% oxygen feeding ratio is illustrated in Fig. 10b. Both plasma reactors showed a slight increase in energy yield from a gap distance of 0.25 mm to 0.50 mm, with maximum energy yield obtained at an intermediate distance of 0.5 mm. However, a sharp drop in energy yield was observed as the gap distance was increased to 0.75 mm. The obtained results are consistent with the trend of production rate shown in Fig. 9b. Conversely, energy cost decreased when the gap distance increased from 0.25 to 0.5 mm, reaching a minimum of 0.5 mm, and then began to increase again in both types of reactors.

To assess the feasibility of plasma-assisted nitrogen fertilizer production from laboratory to farm, it is essential to estimate the energy yield and energy cost during the manufacturing process. The energy cost and energy yield are inversely related as higher energy yield results in more NO_x production per unit of energy input, leading to a lower energy cost per unit of NO_x produced. Conversely, higher energy cost means lower energy yield, as more energy is required to produce the same amount of NO_x . Hence, balancing energy cost and energy yield is crucial to optimize NO_x synthesis [19, 72]. Various industrial nitrogen fixation methods were compared with plasma-assisted nitrogen fixation techniques in terms of energy cost, and the results are presented in Table 1. Estimating energy cost and energy yield can facilitate the optimization of process conditions and innovative reactor design in the future. The purpose of the results presented in this study is not to assert that they represent the optimal outcome. Rather, the intent is to demonstrate that utilizing micrometer-sized electrodes can substantially decrease the energy expenditure associated with the technology utilized. Because energy cost is a critical factor in determining the financial cost of the plasma fertilizer industry.

Importance of Pyramid-shaped Micro-electrode for Nitrogen Fixation

Sharp ends play a crucial role in promoting charge injection in various applications such as electrical discharge machines, field emission devices, and gas discharges [82]. This is because sharp tips or edges concentrate the electric field, leading to a high surface charge density and enhancing the probability of vibrational excitation or ionization of the surrounding gas molecules [82]. Graphical representation of flat and

Table 1 A comparative summary of our work with both conventional industrial nitrogen fixation methods and recent plasma-assisted nitrogen fixation methods

Process	Input	Output	Concentration [mg/L]	E_{cost} [GJ/tN]	References
Birkeland Eyde	Air	NO_3^-	Industrial	400	[7]
Frank caro	CaC_2, N_2	$CaCN_2$	Industrial	250	[7]
Habers-Bosch	$Coal, N_2$	NH_3	Industrial	100	[7]
Habers-Bosch	CH_4, N_2	NH_3	Industrial	18.6	[7]
MW plasma	$O_2, N_2/MoO_3$	NO	123	28	[73]
Rotating gliding arc	Air	NO	36.90	497	[20]
Rotating gliding arc	Air	NO	5.74	48	[20]
Gliding arc	O_2, N_2	NO	4.8	1714	[74]
Gliding arc	O_2, N_2	NO	17.4	103	[24]
Propeller arc	Air	NO	8.2	253	[75]
Gliding arc	N_2, O_2	NO	16.58	330	[76]
Transient spark	N_2, O_2	NO, NO_2	29	614	[77]
Surface DBD	N_2, O_2	NO	18.28	1108	[38]
DBD	$N_2, O_2/BaTiO_2$	NO_2	24.62	347	[78]
Packed DBD	$N_2, O_2/Al_2O_3$	NO, NO_2	6.6	1296	[79]
Plasma Jet (DBD)	Air, H_2O	NH_4^+	12	826	[6]
DBD	Air, H_2O	NO_3^-	1	619	[61]
Plasma jet (DBD)	Dry air	NO, NO_2	2.05	617	[80]
Pulsed arc	N_2, O_2	NO, NO_2	1.2	1080	[65]
Pulsed DBD	air	NO	5	286	[81]
DBD	N_2, O_2	NO, NO_2	13.18	480	Here
μ -electrode DBD	N_2, O_2	NO, NO_2	20.83	327	Here

pyramid μ -electrode DBD and their electric field representation is shown in Fig. 11. The electric field around a flat electrode is uniform due to its consistent surface, and the charge density is inversely proportional to the area of curvature of the surface [83]. Thus, sharp edges with small curvature have higher charge density, resulting in a stronger electric field at the tip where the density of electrons is larger [84]. The velocity of ions, which governs the rate of secondary electron emission, is impacted by the strength of the electric field. Thus, the process of secondary emission may be more intense around sharp points where the electric field has accumulated [82]. Pyramid μ -electrodes provide a high rate of secondary electron emission and field emission due to the high intensity of the local electric field. Furthermore, it is reported that strong electric field can enhance electron density and electron temperature [82]. These energies are being transferred to the neutral nitrogen molecules during the electron impact collisions. Before the utilization of the pyramid-shaped tip, there were several attempts were done at conical-shaped tips in certain applications but these conical tips suffered from thermal damage after only a few hours of use. In contrast, the pyramid-shaped tip appears to be much more resilient to thermal damage. This increased durability and resistance to thermal damage make the pyramid-shaped tip a more reliable and effective HV electrode.

The ratio of vibrational temperature to rotational temperature has been shown to be a crucial factor in plasma-assisted nitrogen fixation. A higher value of this ratio is more

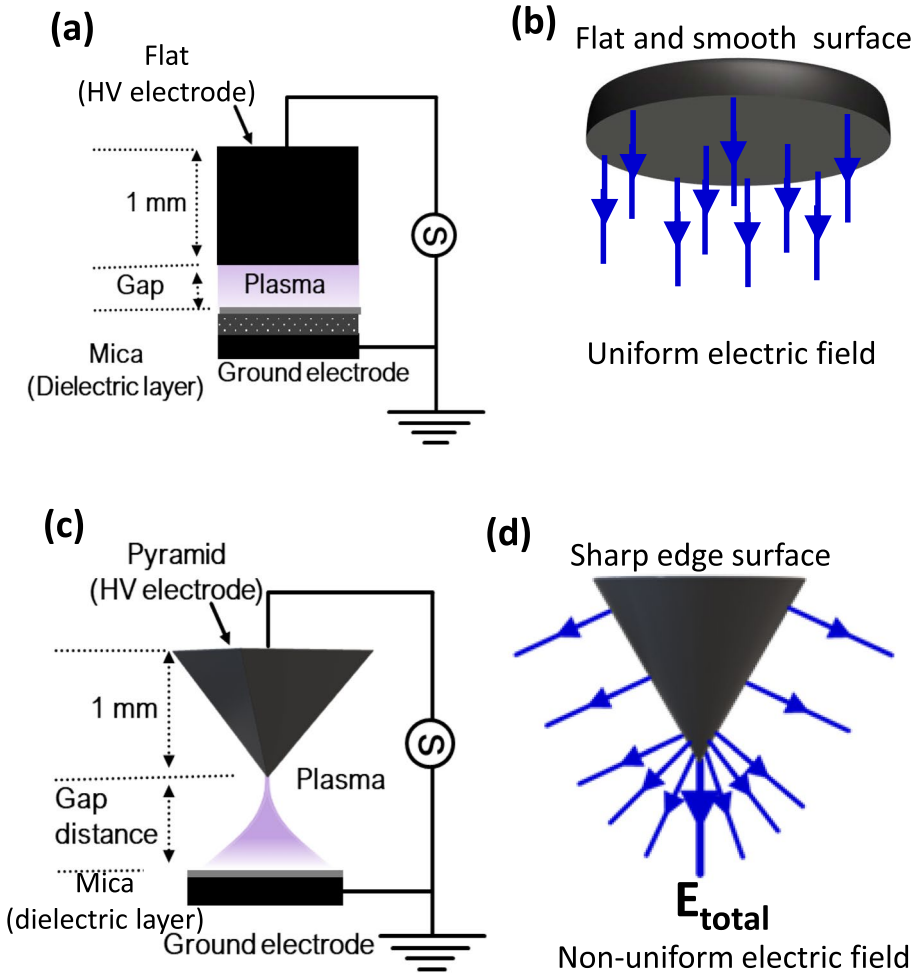


Fig. 11 Schematic of a DBD on **a** flat electrode and **b** electric field representation. **c** Schematic of a DBD on a pyramid μ -electrode and **d** electric field representation

favorable for the process [59, 85]. The results presented in Fig. 7 suggest that a higher vibrational temperature and lower rotational temperature in the pyramid μ -electrode can lead to a more efficient nitrogen fixation process. Also, the higher electric field in the pyramid μ -electrode plasma promotes collisions between dense energetic electrons and neutral molecules, resulting in more energy being transferred to the nitrogen molecules. This increased energy transfer leads to higher nitrogen bond breakdown rate, ionization, or higher population of vibrationally excited molecules. Additionally, the sharp tips or edges on electrodes can facilitate the formation of streamers or filaments in the plasma, which are known to enhance the plasma volume and increase the residence time of reactive species, thereby promoting the overall efficiency of the nitrogen fixation process.

Conclusions

In this research paper, a novel approach to nitrogen fixation using a charge injector in dielectric barrier discharge is proposed. Compared to a conventional flat electrode, the pyramid μ -electrode reactor produces more vibrationally excited nitrogen species plasma effluent gas. The injector takes advantage of the high-intensity local electric fields generated by a pyramid-shaped μ -electrode to increase the rate of secondary electron emission. Experimental results demonstrate that the pyramid μ -electrode plasma is a highly energy-efficient and cost-effective method of nitrogen fixation, achieving high conversion rates at low energy input. Despite requiring slightly more operational power, the pyramid μ -electrode plasma generates up to 58% more NO_x with 32% less energy cost. The study also found that admixing between 60% to 70% of oxygen in the nitrogen feeding gas provides a maximum output of gas phase nitrogen oxides. In short, due to its energy efficiency, cost-effectiveness, and high conversion rates, the pyramid μ -electrode has significant potential for nitrogen fixation in the sustainable and localized micro-fertilizer industry.

Author Contributions PL: Conceptualization, investigation, software, writing the original draft, review, and editing. NP: Investigation, review. EV.R: Review, editing, and resources. VH: Conceptualization, writing, review, editing, supervision, resources, project administration, funding acquisition.

Funding This work is supported by the ERC Synergy Grant “Surface-CONfined fast modulated Plasma for Process and Energy intensification” (SCOPE), from the European Commission, with Grant No. 810182.

Data Availability The data that support the findings of this study are available from the submitting author upon reasonable request.

Declarations

Conflict of interest We declare that the authors have no competing interests or other interests that might be perceived to influence the results reported in this paper.

Ethical approval This experiment does not involve the use of any humans or animals.

Open Access This article is licensed under a Creative Commons Attribution 4.0 International License, which permits use, sharing, adaptation, distribution and reproduction in any medium or format, as long as you give appropriate credit to the original author(s) and the source, provide a link to the Creative Commons licence, and indicate if changes were made. The images or other third party material in this article are included in the article’s Creative Commons licence, unless indicated otherwise in a credit line to the material. If material is not included in the article’s Creative Commons licence and your intended use is not permitted by statutory regulation or exceeds the permitted use, you will need to obtain permission directly from the copyright holder. To view a copy of this licence, visit <http://creativecommons.org/licenses/by/4.0/>.

References

1. Godswill AG, Somtochukwu IV, Ikechukwu AO, Kate EC (2020) Health benefits of micronutrients (vitamins and minerals) and their associated deficiency diseases: a systematic review. *Int J Food Sci* 3:1–32
2. Grandy AS, Loecke TD, Parr S, Robertson GP (2006) Long-term trends in nitrous oxide emissions, soil nitrogen, and crop yields of till and no-till cropping systems. *J Environ Qual* 35:1487–1495
3. Lamichhane P et al (2021) Low-temperature plasma-assisted nitrogen fixation for corn plant growth and development. *Int J Mol Sci* 22:5360

4. Patil BS et al (2018) Plasma assisted nitrogen oxide production from air: using pulsed powered gliding arc reactor for a containerized plant. *AIChE J* 64:526–537
5. Eyde HS (1909) The manufacture of nitrates from the atmosphere by the electric arc-birkeland-eyde process. *J R Soc Arts* 57:568–576
6. Lamichhane P et al (2020) Plasma-assisted nitrogen fixation in water with various metals. *Reaction Chem Eng* 5:2053–2057
7. Rouwenhorst KH et al (2020) Plasma-driven catalysis: green ammonia synthesis with intermittent electricity. *Green Chem* 22:6258–6287
8. Cherkasov N, Ibhaden A, Fitzpatrick P (2015) A review of the existing and alternative methods for greener nitrogen fixation. *Chem Eng Process* 90:24–33
9. Erisman JW, Sutton MA, Galloway J, Klimont Z, Winiwarter W (2008) How a century of ammonia synthesis changed the world. *Nat Geosci* 1:636–639
10. Peng P et al (2018) A review on the non-thermal plasma-assisted ammonia synthesis technologies. *J Clean Prod* 177:597–609
11. Patil B, Wang Q, Hessel V, Lang J (2015) Plasma n₂-fixation: 1900–2014. *Catal Today* 256:49–66
12. Lamichhane P et al (2020) Sustainable nitrogen fixation from synergistic effect of photo-electrochemical water splitting and atmospheric pressure n₂ plasma. *Plasma Sources Sci Technol* 29:045026
13. Lin L, Xu H, Gao H, Zhu X, Hessel V (2020) Plasma-assisted nitrogen fixation in nanomaterials: fabrication, characterization, and application. *J Phys D Appl Phys* 53:133001
14. Patil BS et al (2020) Deciphering the synergy between plasma and catalyst support for ammonia synthesis in a packed dielectric barrier discharge reactor. *J Phys D Appl Phys* 53:144003
15. Hessel V et al (2023) Circular bioprocess for phosphorus nutrient recovery to grow lettuce in lunar space. *Green Chem* 2:63
16. Miao Y, Yokochi A, Jovanovic G, Zhang S, von Jouanne A (2023) Application-oriented non-thermal plasma in chemical reaction engineering: a review. *Green Energy Resour* 6:100004
17. Li W et al (2023) Sustainable nitrogen fixation to produce ammonia by electroreduction of plasma-generated nitrite. *ACS Sustain Chem Eng* 2:396
18. Tsonev I, O'Modhrain C, Bogaerts A, Gorbanev Y (2023) Nitrogen fixation by an arc plasma at elevated pressure to increase the energy efficiency and production rate of no x. *ACS Sustain Chem Eng* 11:1888–1897
19. Hessel V, Anastasopoulou A, Wang Q, Kolb G, Lang J (2013) Energy, catalyst and reactor considerations for (near)-industrial plasma processing and learning for nitrogen-fixation reactions. *Catal Today* 211:9–28
20. Muzammil I et al (2021) A novel energy efficient path for nitrogen fixation using a non-thermal arc. *RSC Adv* 11:12729–12738
21. Dinh DK, Muzammil I, Kang WS, Kim D, Lee DH (2021) Reducing energy cost of in situ nitrogen fixation in water using an arc-dbd combination. *Plasma Sources Sci Technol* 30:055020
22. Muzammil I et al (2021) Plasma catalyst-integrated system for ammonia production from h₂o and n₂ at atmospheric pressure. *ACS Energy Lett* 6:3004–3010
23. Lamichhane P et al (2022) Non-thermal argon plasma jets of various lengths for selective reactive oxygen and nitrogen species production. *J Environ Chem Eng* 10:107782
24. Patil B, Wang Q, Hessel V, Lang J (2016) Plasma-assisted nitrogen fixation reactions. In: *Alternative energy sources for green chemistry*, pp 296
25. Anastasopoulou A et al (2020) Eco-efficiency analysis of plasma-assisted nitrogen fixation. *J Phys D Appl Phys* 53:234001
26. Veerana M et al (2021) Plasma-mediated enhancement of enzyme secretion in *aspergillus oryzae*. *Microb Biotechnol* 14:262–276
27. Ranieri P et al (2021) Plasma agriculture: review from the perspective of the plant and its ecosystem. *Plasma Process Polym* 18:2000162
28. Chuesaard T et al (2023) Different effects of reactive species generated from chemical donors on seed germination, growth, and chemical contents of *oryza sativa* l. *Plants* 12:765
29. Amri D, Nawawi Z, Jambak MI (2019) The comparison between types of electrodes in dielectric barrier discharge (dbd) plasma for obtaining potable water: a review. *IOP Conf Ser Mater Sci Eng* 620:012091
30. Gilbert B, Dickenson A, Walsh JL, Hasan MI (2022) Mutual interaction among multiple surface barrier discharges. *Plasma Process Polym* 19:2100181
31. Takayama M et al (2006) Ozone generation by dielectric barrier discharge for soil sterilization. *Thin Solid Films* 506:396–399
32. Liu Z-J et al (2014) A large-area diffuse air discharge plasma excited by nanosecond pulse under a double hexagon needle-array electrode. *Spectrochim Acta Part A Mol Biomol Spectrosc* 121:698–703

33. Liu Z-J et al (2013) The effect of dielectric thickness on diffuse nanosecond dielectric barrier discharges using a needle array-plate electrode configuration in the air at atmospheric pressure. *J Appl Phys* 113:233305
34. Takaki K, Shimizu M, Mukaigawa S, Fujiwara T (2004) Effect of electrode shape in dielectric barrier discharge plasma reactor for nox removal. *IEEE Trans Plasma Sci* 32:32–38
35. Bayram S, Arndt P, Freamat M (2015) Rotational spectra of n₂⁺: an advanced undergraduate laboratory in atomic and molecular spectroscopy. *Am J Phys* 83:867–872
36. Ghimire B et al (2017) The effect of the gap distance between an atmospheric-pressure plasma jet nozzle and liquid surface on oh and n₂ species concentrations. *Phys Plasmas* 24:073502
37. St Hill N, Turner G (2011) Calibration of a fourier transform infrared spectrometer for hydrogen peroxide vapour measurement. *Anal Methods* 3:1901–1905
38. Pei X, Gidon D, Yang Y-J, Xiong Z, Graves DB (2019) Reducing energy cost of nox production in air plasmas. *Chem Eng J* 362:217–228
39. Lamichhane P et al (2019) Control of hydrogen peroxide production in plasma activated water by utilizing nitrification. *J Phys D Appl Phys* 52:265206
40. Pourali N et al (2023) Study of plasma parameters and gas heating in the voltage range of nondischarge to full-discharge in a methane-fed dielectric barrier discharge. *Plasma Processes Polym* 20:2200086
41. Liang J, Jiao Y, Jaroniec M, Qiao SZ (2012) Sulfur and nitrogen dual-doped mesoporous graphene electrocatalyst for oxygen reduction with synergistically enhanced performance. *Angew Chem* 124:11664–11668
42. Goodings J, Bohme D, Ng C-W (1979) Detailed ion chemistry in methane oxygen flames. ii. Negative ions. *Combust Flame* 36:45–62
43. McKay K, Iza F, Kong M (2010) Excitation frequency effects on atmospheric-pressure helium rf microplasmas: plasma density, electron energy and plasma impedance. *Eur Phys J D* 60:497–503
44. Rahman A et al (2004) Absolute UV and VUV emission in the 110–400 nm region from 13.56 mhz driven hollow slot microplasmas operating in open air. *Plasma Sources Sci Technol* 13:537
45. Adhikari BC, Lamichhane P, Lim JS, Nguyen LN, Choi EH (2021) Generation of reactive species by naturally sucked air in the ar plasma jet. *Res Phys* 30:104863
46. Thomas S, Nalini S, Kumar KR (2017) Microwave plasma-assisted ald of al₂o₃ thin films: a study on the substrate temperature dependence of various parameters of interest. *Appl Phys A* 123:1–7
47. Hrycak B, Jasiński M, Mizeraczyk J (2012) Spectroscopic characterization of nitrogen plasma generated by waveguide-supplied coaxial-line-based nozzleless microwave source. *J Phys Conf Ser* 406:012037
48. Hosseini SI, Mohsenimehr S, Hadian J, Ghorbanpour M, Shokri B (2018) Physico-chemical induced modification of seed germination and early development in artichoke (*cynara scolymus* l.) using low energy plasma technology. *Phys Plasmas* 25:013525
49. Bruggeman P et al (2009) Characterization of a direct dc-excited discharge in water by optical emission spectroscopy. *Plasma Sources Sci Technol* 18:025017
50. Hong YC, Kang WS, Hong YB, Yi WJ, Uhm HS (2009) Atmospheric pressure air-plasma jet evolved from microdischarges: eradication of *E. coli* with the jet. *Phys Plasmas* 16:123502
51. Xiao D et al (2014) Characteristics of atmospheric-pressure non-thermal n₂ and n₂/o₂ gas mixture plasma jet. *J Appl Phys* 115:033303
52. Deng X, Nikiforov AY, Vanraes P, Leys C (2013) Direct current plasma jet at atmospheric pressure operating in nitrogen and air. *J Appl Phys* 113:023305
53. Gazeli K, Svarnas P, Held B, Marlin L, Clement F (2015) Possibility of controlling the chemical pattern of he and ar “guided streamers” by means of n₂ or o₂ additives. *J Appl Phys* 117:093302
54. Mavadat M, Ricard A, Sarra-Bournet C, Laroche G (2011) Determination of rotational and vibrational excitations of n₂ (b, v⁺) and n₂ (c, v⁻) states in n₂ microwave discharges using visible and ir spectroscopy. *J Phys D Appl Phys* 44:155207
55. Kolb JF et al (2008) Cold atmospheric pressure air plasma jet for medical applications. *Appl Phys Lett* 92:241501
56. Rezaei F, Abbasi-Firouzjah M, Shokri B (2014) Investigation of antibacterial and wettability behaviours of plasma-modified pmma films for application in ophthalmology. *J Phys D Appl Phys* 47:085401
57. Stancu G-D, Kaddouri F, Lacoste D, Laux C (2010) Atmospheric pressure plasma diagnostics by oes, crds and talif. *J Phys D Appl Phys* 43:124002
58. Ghimire B et al (2018) An atmospheric pressure plasma jet operated by injecting natural air. *Appl Phys Lett* 113:194101
59. Roy NC et al (2023) Mechanisms of reducing energy costs for nitrogen fixation using air-based atmospheric dbd plasmas over water in contact with the electrode. *Chem Eng J* 3:141844

60. Joh HM, Choi JY, Kim SJ, Chung T, Kang T-H (2014) Effect of additive oxygen gas on cellular response of lung cancer cells induced by atmospheric pressure helium plasma jet. *Sci Rep* 4:1–9
61. Liu Z, Tian Y, Niu G, Wang X, Duan Y (2021) Direct oxidative nitrogen fixation from air and h₂o by a water falling film dielectric barrier discharge reactor at ambient pressure and temperature. *Chemsuschem* 14:1507–1511
62. Kim Y, Stange SM, Rosocha LA, Ferreri VW (2005) Enhancement of propane flame stability by dielectric barrier discharges. *J Adv Oxidation Technol* 8:188–192
63. Haruyama T et al (2016) Non-catalyzed one-step synthesis of ammonia from atmospheric air and water. *Green Chem* 18:4536–4541
64. Schulz GJ (1962) Vibrational excitation of nitrogen by electron impact. *Phys Rev* 125:229
65. Namihira T, Katsuki S, Hackam R, Akiyama H, Okamoto K (2002) Production of nitric oxide using a pulsed arc discharge. *IEEE Trans Plasma Sci* 30:1993–1998
66. Winter LR, Chen JG (2021) N₂ fixation by plasma-activated processes. *Joule* 5:300–315
67. Attri P et al (2015) Generation mechanism of hydroxyl radical species and its lifetime prediction during the plasma-initiated ultraviolet (uv) photolysis. *Sci Rep* 5:1–8
68. Uhm HS, Ki SH, Baik KY, Choi EH (2018) Influence of oxygen on generation of reactive chemicals from nitrogen plasma jet. *Sci Rep* 8:9318
69. Vervloessem E, Gorbanev Y, Nikiforov A, De Geyter N, Bogaerts A (2022) Sustainable no_x production from air in pulsed plasma: elucidating the chemistry behind the low energy consumption. *Green Chem* 24:916–929
70. Ghazali NA et al (2010) Transformation of nitrogen dioxide into ozone and prediction of ozone concentrations using multiple linear regression techniques. *Environ Monit Assess* 165:475–489
71. Crutzen PJ (2016) The influence of nitrogen oxides on atmospheric ozone content. *Paul J Crutzen* 6:108–116
72. Li S, Medrano JA, Hessel V, Gallucci F (2018) Recent progress of plasma-assisted nitrogen fixation research: a review. *Processes* 6:248
73. Mutel B, Dessaux O, Goudmand P (1984) Energy cost improvement of the nitrogen oxides synthesis in a low pressure plasma. *Revue de physique appliquée* 19:461–464
74. Vervloessem E, Aghaei M, Jardali F, Hafezkhianani N, Bogaerts A (2020) Plasma-based n₂ fixation into no_x: insights from modeling toward optimum yields and energy costs in a gliding arc plasmatron. *ACS Sustain Chem Eng* 8:9711–9720
75. Pei X, Gidon D, Graves DB (2019) Specific energy cost for nitrogen fixation as no_x using dc glow discharge in air. *J Phys D Appl Phys* 53:044002
76. Wang W, Patil B, Heijkens S, Hessel V, Bogaerts A (2017) Nitrogen fixation by gliding arc plasma: better insight by chemical kinetics modelling. *Chemsuschem* 10:2145–2157
77. Janda M, Martišovič V, Hensel K, Machala Z (2016) Generation of antimicrobial no_x by atmospheric air transient spark discharge. *Plasma Chem Plasma Process* 36:767–781
78. Ma Y, Wang Y, Harding J, Tu X (2021) Plasma-enhanced n₂ fixation in a dielectric barrier discharge reactor: effect of packing materials. *Plasma Sources Sci Technol* 30:105002
79. Patil B et al (2016) Low temperature plasma-catalytic no_x synthesis in a packed dbd reactor: effect of support materials and supported active metal oxides. *Appl Catal B* 194:123–133
80. Hao X et al (2014) Nitric oxide generation with an air operated non-thermal plasma jet and associated microbial inactivation mechanisms. *Plasma Processes Polym* 11:1044–1056
81. Korolev YD, Frants OB, Landl NV, Suslov AI (2012) Low-current plasmatron as a source of nitrogen oxide molecules. *IEEE Trans Plasma Sci* 40:2837–2842
82. Pourali N, Hessel V, Rebrov EV (2022) The effects of pulse shape on the selectivity and production rate in non-oxidative coupling of methane by a micro-dbd reactor. *Plasma Chem Plasma Process* 42:619–640
83. Matehkolaei MJ, Asrami AN (2017) The review on the charge distribution on the conductor surface. *Eur J Phys Educ* 4:1–6
84. Liu P et al (2021) Tip-enhanced electric field: a new mechanism promoting mass transfer in oxygen evolution reactions. *Adv Mater* 33:2007377
85. Raizer YP, Allen JE (1991) *Gas discharge physics* Vol. 1 (Springer)